

Localization due to topological stochastic disorder in active networks

Dekel Shapira, Dganit Meidan, and Doron Cohen

Department of Physics, Ben-Gurion University of the Negev, Beer-Sheva 84105, Israel



(Received 14 March 2018; published 5 July 2018)

An active network is a prototype model in nonequilibrium statistical mechanics. It can represent, for example, a system with particles that have a self-propulsion mechanism. Each node of the network specifies a possible location of a particle and its orientation. The orientation (which is formally like a spin degree of freedom) determines the self-propulsion direction. The bonds represent the possibility to make transitions: to hop between locations or to switch the orientation. In systems of experimental interest (Janus particles), the self-propulsion is induced by illumination. An emergent aspect is the topological stochastic disorder (TSD). It is implied by the nonuniformity of the illumination. In technical terms the TSD reflects the local nonzero circulations (affinities) of the stochastic transitions. This type of disorder, unlike a nonhomogeneous magnetic field, is non-Hermitian and can lead to the emergence of a complex relaxation spectrum. It is therefore dramatically distinct from the conservative Anderson-type or Sinai-type disorder. We discuss the consequences of having TSD. In particular we illuminate three different routes to underdamped relaxation and show that localization plays a major role in the analysis. Implications of the bulk-edge correspondence principle are addressed too.

DOI: [10.1103/PhysRevE.98.012107](https://doi.org/10.1103/PhysRevE.98.012107)

I. INTRODUCTION

Gas that consists of particles that perform self-propelled stochastic motion is a novel paradigm in statistical mechanics [1–4]. Many publications have focused on the implied hydrodynamic properties of such active matter, for example, its pressure [5], odd viscosity (for spinning particles) [6], or the similar cross-stream migration behavior of the particles [7]. The aspect that we would like to address is not related to the nonequilibrium steady state (NESS) of the active system, but rather to its relaxation dynamics.

To be specific we highlight, as an example, a system that consists of Janus particles [8–10]. Those are spherical-like nanoparticles, coated at each of their two hemispheres with different materials. Immersed in solution and radiated with light, they produce self-propelled motion. If a microgear is placed in such an active solution it will rotate [11].

Figure 1(a) shows a caricature of a Janus particle in a one-dimensional system. In this caricature the particle can be anywhere along the horizontal axis (n is an integer) and can face either to the right or to the left ($s = \uparrow, \downarrow$). The illumination provides the self-propulsion mechanism. For a given orientation the particle executes a biased stochastic random walk: The motion is biased to the right (left) if the particle is facing the right (left). Formally, the orientation of the particle is like a spin degree of freedom and below we refer to it as polarization.

Janus particles that form such an active system can be placed in a disordered background environment [12]. This kind of disorder is derived from a potential and as such is termed conservative. Irrespective of that, the illumination might be nonhomogeneous. This nonhomogeneity provides a different type of disorder. As explained below, such a type of inherently different disorder is topological rather than conservative.

Dynamical simulation. In order to show the importance of studying the relaxation dynamics let us discuss the simulation

that is provided by Fig. 2. In an actual experiment the particles occupy a two-dimensional strip and some ordering field encourages them to have either left or right polarization. We prepare, at time $t = 0$, a solution that has a uniform density of Janus particles, but with modulated polarization. In the figure, the color code is such that red and blue regions occupy right-polarized ($s = \uparrow$) and left-polarized ($s = \downarrow$) particles, respectively. The dynamics is formally described by a stochastic rate equation

$$\frac{d}{dt} \mathbf{p} = \mathbf{W} \mathbf{p}, \quad (1)$$

where \mathbf{p} is vector of probabilities and \mathbf{W} is a real asymmetric matrix that is determined by the transition rates. Due to the illumination, the right- (left-) polarized particles execute self-propelled stochastic motion that is biased to the right (left). In the absence of disorder we see that the relaxation of the system becomes underdamped instead of overdamped if the strength of the illumination ϕ exceeds a critical value. We also see that in the presence of disorder both the steady state and the relaxation scenario become very different.

Complex spectrum. In order to understand the relaxation of a stochastic system, as in the simulation discussed above, we have to inspect its relaxation modes. These are the eigenvectors of the real \mathbf{W} matrix of Eq. (1). They decay in time as $\exp(-\lambda_r t)$, where the $\{-\lambda_r\}$ are the associated eigenvalues. The relaxation becomes underdamped, meaning that it exhibits oscillations in time, if some of the λ_r acquire an imaginary part. Formally, we are dealing with the physics of real non-Hermitian matrices, where the spectrum might become complex [13–24].

Observations. Our objective is to provide a precise quantitative framework for the analysis of relaxation in active networks. In particular, we are interested in the implications of disorder and the possible manifestation of localization effect in the relaxation modes of such systems. We are going to explore

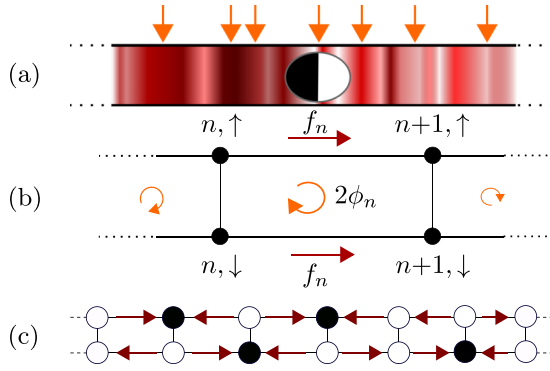


FIG. 1. Model geometry. (a) Janus particle in a one-dimensional random environment. The nonuniform illumination (arrows) induce self-propulsion in the direction of the head (white). The orientation of the head is called below polarization. (b) Lattice modeling of the system. Each node represents a possible location n and possible polarization $s = \uparrow, \downarrow$. One tile of the lattice is plotted. The system is composed of N tiles with periodic boundary conditions. The transition rates along the vertical bonds are $w = 1$ in both directions, representing random flips of polarization. The horizontal bonds are biased: The stochastic field there \mathcal{E} is written as the sum of a drift f_n and a self-propulsion term ϕ_n . The latter reflects that we are dealing with an active network. (c) Illustration of a representative segment of the lattice. The black sites are those that serve as sinks for the stochastic flow in the presence of strong disorder. They support the floor-level relaxation modes.

different routes towards underdamped relaxation. The traditional way of getting underdamped relaxation is to introduce bias that causes the particle to drift in one direction. In the present study we are going to discuss the possibility to get underdamped relaxation due to self-propulsion. We are going to see that uniform illumination requires a finite threshold value, unlike nonuniform illumination, which induces complexity as soon as it is introduced. We will see that stochastic disorder can either stabilize or destabilize the overdamped modes, depending on whether it is conservative or topological.

Active network. We deal with particles that execute self-propelled motion. The formal modeling is in terms of a network; for our specific configuration it is the N -tile lattice of Fig. 1(b). The network is described by the matrix \mathbf{W} of Eq. (1). On each bond b we define a stochastic field \mathcal{E}_b that indicates how the transitions are biased. We use the notation \mathcal{B}_n for the circulation of \mathcal{E}_b around the n th tile of the network. If all the circulations \mathcal{B}_n are zero, alias detailed balance, we say that the system is conservative. In such a system the NESS is a canonical equilibrium state with zero currents. Nonzero circulations are called affinities and can drive NESS currents.

Topological disorder. In the present work we consider a type of disorder that we call topological stochastic disorder (TSD). It arises due to having a random \mathcal{B}_n and therefore constitutes a generic feature of the active network. This is in contrast with having random \mathcal{E}_b with zero \mathcal{B}_n , which generates conservative disorder. The topological disorder is a type of disorder which is very different from, say, a random magnetic field [25], because it breaks the Hermiticity of \mathbf{W} , leading to the appearance of a complex spectrum. Such a type of disorder, which arises due to nonzero circulations, requires more than one channel, or

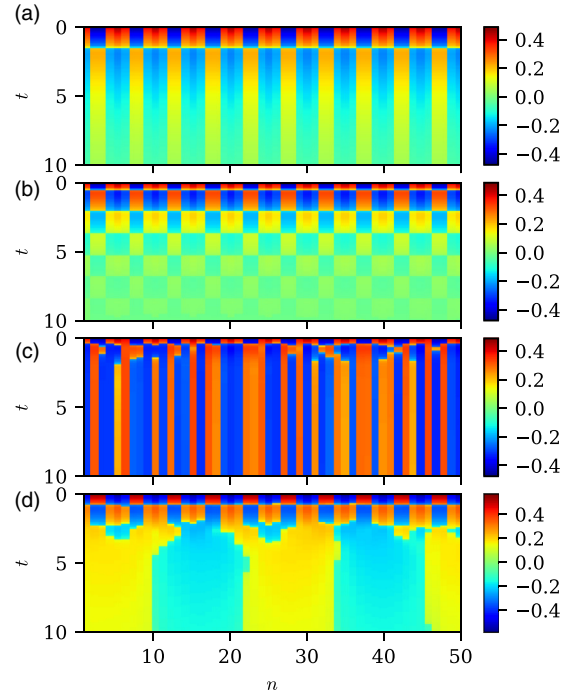


FIG. 2. Simulation of polarization as a function of time. The average polarization D_n at each location n is color coded and imaged as a function of time t . In all the panels the polarization of the initial perpetration is modulated with wave number $k = 2\pi/5$, namely, $p_{n,s} \propto 1 \pm \cos(kn)$. Only 50 sites are displayed. (a) Overdamped oscillations for $\phi = 0.5$ are observed since the self-propulsion is below the critical threshold. (b) For $\phi = 2$, which is above the threshold, one observes underdamped relaxation due to topological symmetry breaking. (c) Once disorder is added, the nonuniform NESS pattern takes over almost immediately. The parameters here are as in Fig. 3. (d) In the latter case we provide an image of the time derivative \dot{D}_n , hence one can resolve how the underdamped relaxation is blurred.

more than one dimension, hence the term topological. In two dimensions, the continuum-space limit of a stochastic random-walk process leads to a diffusion equation. The presence of TSD implies the appearance of a solenoidal random drift field. The effect of the latter has been discussed in [26], where it has been shown that it leads to a slightly superdiffusive spreading.

Floor level. Strong disorder tends to attract the system into sinks, as illustrated in Fig. 1(c). In the case of conservative disorder those sinks are stable minima of the stochastic potential. In the case of TSD the stability of the sinks is marginal. Either way, after a transient time the probability distribution becomes concentrated within this floor level. The term floor level refers to this set of sinks, which supports the slow-relaxation modes of the network.

A. Related studies

1. Topological NESS

The topological nature of the NESS for the model that we are considering, without disorder, has been discussed in [27,28] and a connection has been established with the Su-Schrieffer-Heeger model following the work of [29] on topological boundary modes in isostatic lattices. In the present work we are

not considering the NESS, but rather the relaxation modes and their bulk localization properties due to disorder. We note also that the NESS of similar nondisordered quasi-one-dimensional models has been investigated in the context of traffic with exclusion rules (see, for example, [30,31]). The main focus in the latter case was the formation of a polarization wall due to the entering and the exiting rates at the boundaries.

2. The Sinai model

The minimal model for stochastic motion in a disordered lattice is due to Sinai [32–35]; it is also known as a random walk in a random environment. In the Sinai model the particle can hop between neighboring sites of a chain and the rates of transition are random numbers. This leads, in the absence of bias, to subdiffusion. Above some critical bias the drift velocity becomes nonzero, which is known as the sliding transition.

3. The Hatano-Nelson model

The asymmetry of the \mathbf{W} matrix in Sinai's model can be gauged away, hence it is similar to a Hermitian matrix, and possesses a real spectrum. However, this is not the case if the chain is closed into a ring (i.e., imposing periodic boundary conditions). It has been realized [15–17] that above some critical bias the spectrum becomes complex, and this is termed a delocalization transition. The subtle relation to the sliding transition in Sinai's model was investigated in a later study [22].

4. Anderson localization

The analysis of Sinai's model, which describes random walk in a nonactive disordered environment, is strongly related to studies of Anderson-type localization. It is customary to distinguish between two types of disorder, so-called type I and type II [36,37]. Roughly speaking, the former arises from on-site disorder, while the latter arises from bond disorder, in the senses of resistor network models [38].

B. Outline

We provide a precise definition of the minimal model in Sec. II, where we also review the different types of disorder that can arise in a network. We highlight in Sec. III the different routes to complexity. Section IV provides a detailed account for the breakdown of reality due to self-propulsion in the absence of disorder. Section V explains how the spectrum is affected by the introduction of TSD and why the threshold for complexity diminishes due to the disorder. In Sec. VI we introduce several measures for the characterization of a relaxation mode, which help us gain a deeper insight into the spectrum.

Conservative disorder is responsible for the robustness of reality, meaning that eigenvalues remain real even if not-too-strong circulations are introduced. In contrast, TSD leads to complexity via topological mixing. However, there is a variation: We observe in Sec. VII that strong stochastic disorder, irrespective of its nature, induces lattice dilution, leading to the formation of a floor level. Consequently, the effective dimensionality of the lattice is reduced and a robust reality is gained within this floor level. The topological-index perspective of the disorder and its connection to the floor

level phenomenology are further discussed in Sec. VIII. We summarize the work and discuss the results in Sec. IX.

II. THE MINIMAL MODEL

We consider a minimal configuration for a self-propelled particle in a random environment, namely, we assume that the dynamics takes place on a quasi-one-dimensional grid [see Fig. 1(b)]. If the particle is facing to the right, we say it has right polarization. If its black-white orientation is opposite, we say that it has left polarization. Accordingly, its states $|n,s\rangle$ are defined in terms of position (n is an integer) and spin coordinate ($s = \uparrow, \downarrow$). Below we refer to the system as a lattice that consists of sites. Each two sites with the same index n form a cell and two adjacent cells, along with their connecting bonds, form a tile. The dynamics is described by the rate equation (1). The off-diagonal elements of the \mathbf{W} matrix are the transition rates w (with an appropriate bond index). The diagonal elements $-\gamma$ (with an appropriate state index) are implied by conservation of probability (the sum of each column has to be zero). The matrix \mathbf{W} is given explicitly in Appendix A. The rate of transition between two sites, connected by a bond b , is characterized by a stochastic field

$$\mathcal{E}_b = \ln \left(\frac{w_{\rightarrow b}}{w_{\leftarrow b}} \right) \quad (2)$$

whose sign indicates the preferred sense of transition. Thus the rates on a given bond can be written as $w_b \exp(\pm \mathcal{E}_b/2)$. In the geometry of Fig. 1(b), the vertical bonds represent a random flip of orientation and therefore are characterized by a zero stochastic field. In contrast, the horizontal bonds are biased. The stochastic field on the bond $b = (n,s)$ that connects node $|n,s\rangle$ to $|n+1,s\rangle$ is conveniently written as a sum of drift and self-propulsion terms, namely,

$$\begin{aligned} \mathcal{E}_{n,\uparrow} &= f_n + \phi_n, \\ \mathcal{E}_{n,\downarrow} &= f_n - \phi_n. \end{aligned} \quad (3)$$

The activity of the network is reflected in having nonzero circulations, also known as affinities (analogous to magnetic field). The circulation of the n th tile is

$$\mathcal{B}_n = 2\phi_n. \quad (4)$$

If all the circulations are zero, a gauge transformation can be used to show that \mathbf{W} is similar to a symmetric matrix \mathbf{H} , hence all the eigenvalues are real, as for Hermitian Hamiltonians. Otherwise we are dealing with the physics of non-Hermitian matrices, where the spectrum might become complex [13–24].

A. Model parameters

The motion of the Janus particles is regarded as a hopping process between sites of a network [see Fig. 1(b)]. The unbiased transition rates are w_b . In the continuum limit we get diffusion with the coefficient $\mathcal{D} \propto w_b$. We assume for simplicity that all the w_b are the same. Some further remarks about the implication of having different rates for the vertical flips are presented in Appendix B.

The motion in Fig. 1(a) is controlled by a nonzero-average drift field \bar{f} and a nonzero-average self-propulsion $\bar{\phi}$. Disorder

TABLE I. Different types of disorder.

Type	Alias	Relevant models	Comments
type I	diagonal disorder	Anderson model (random potential)	might have a mobility edge
type II	bond disorder	Debye model and random resistor network	might lead to a percolation transition
MFD	phase disorder	Anderson model with random vector potential	topological aspect is not pronounced
CSD		Sinai model of random stochastic transitions	reduces to type I via gauge transformation
RSD	sign disorder	random excitatory and inhibitory connections	non-Hermiticity cannot be gauged away
TSD		generic active networks	non-Hermiticity is of topological origin

may arise due to the nonhomogeneity of the background environment or due to the nonhomogeneity of the illumination source. Respectively, we distinguish between conservative stochastic disorder (CSD), for which the f_n acquire a random term $\in [-\sigma_f, \sigma_f]$, and TSD, for which the ϕ_n acquire a random term $\in [-\sigma_\phi, \sigma_\phi]$. Accordingly, the model parameters are \bar{f} , $\bar{\phi}$, σ_f , and σ_ϕ and the length of the sample, N .

B. Types of disorder

It is customary to distinguish between two types of disorder, so-called type I and type II [36,37]. We explain these terms in the present context and highlight a different type of disorder. The different types of disorder are summarized in Table I.

Random f_n , as in the Sinai model (alias a random walk in a random environment) [32–35], translates, under gaugelike transformation, into type-I disorder [17], which is a diagonal on-site disorder as in the Anderson model (electron in a random potential). We refer to it as CSD.

Random w_b , as in random resistor network models [38] or as in the Debye model (balls connected by nonidentical springs), translates into type-II disorder, which is an off-diagonal bond disorder. The latter type of disorder can lead to a percolationlike transition that affects the relaxation modes [22] and we will not consider it further.

In the present work we consider a type of disorder that we refer to as TSD. This type of disorder originates from having random ϕ_n and, unlike CSD, cannot be gauged away. We note that, physically, TSD arises naturally also in situations other than active particles. For example, the affinities \mathcal{B}_n may reflect nonconservative drift fields that are induced by electromotive forces.

With the substitution $\phi_n \mapsto i\phi_n$ our TSD becomes magnetic-field disorder (MFD), which has been discussed in the past (see, e.g., [25] and references therein). One should be aware that there is an essential difference between TSD and MFD: The latter has qualitatively the same effect as the usual type-I Anderson disorder, while TSD makes the spectrum complex.

Another type of non-Hermitian disorder that has been discussed in the literature is random sign disorder (RSD) (see [21] and references therein). It concerns biological networks, where the w_b have random sign, corresponding to random excitatory and inhibitory connections. It should be realized that RSD has nothing to do with topology: The model of [21] is a single-channel tight-binding model with near-neighbor transitions. In contrast, TSD requires at least two channels, as in the case of a random magnetic field. Also, it should be realized that the strength of TSD, unlike that of RSD, is tunable.

III. DIFFERENT ROUTES TO COMPLEXITY

We first recall the simplest result for the relaxation spectrum of particles that diffuse in a single-channel biased ring. This result illustrates the delocalization route to complexity. For any nonzero bias the spectrum becomes fully complex $\lambda = \mathcal{D}k^2 + ivk$, where k is the wave number, \mathcal{D} is the diffusion coefficient, and v is the drift velocity. A similar expression applies for a tight-binding model (see, e.g., [23]).

The spectrum of a one-channel disordered ring, in the absence of bias, is real. With added bias, some eigenvalues become complex. The complexity appears only if the bias exceeds a finite threshold, alias the delocalization threshold [15,16]. The eigenstates that correspond to real eigenvalues are then localized, while those that are associated with complex eigenvalues are extended. As discussed in [23], the low relaxation modes (small $\text{Re}[\lambda]$) get delocalized first, while the high-lying relaxation modes remain real.

We consider a two-channel ring of N unit cells with periodic boundary conditions [Fig. 1(b)]. This is the simplest example for an active network; we are going to find two additional routes to complexity that have to do with the nontrivial topology of the model. We distinguish between the circulation that is induced by the drift and the circulation that reflects the self-propulsion, namely,

$$\sum f_n \equiv N\bar{f}, \quad (5)$$

$$\sum \mathcal{B}_n \equiv 2N\bar{\phi}, \quad (6)$$

where $\mathcal{B}_n = 2\phi_n$ is the affinity of the n th tile. For simplicity we assume that all the couplings are identical ($w_b = 1$ for any b). In the absence of disorder, \mathbf{W} is translationally symmetric and can be written very simply using momentum and spin operators

$$\mathbf{W} = (\sigma_x - 1) + \sum_{\pm} e^{\pm(\bar{f} + \bar{\phi}\sigma_z)/2} (e^{\mp ip} - 1). \quad (7)$$

The Pauli operator σ_x term induces the random change in the propulsion direction (vertical transitions in Fig. 1), the \pm terms generate the forward and backward transitions, and the -1 terms provide the diagonal elements (decay rates) that are required for conservation of probability. The operators $e^{\pm ip}$ and σ_i are written using explicit Dirac notation in Appendix A. We are now in position to explain how each of the parameters of the model (\bar{f} , $\bar{\phi}$, σ_f , and σ_ϕ) affects the complexity of the spectrum.

Conservative stochastic disorder. Conservative stochastic disorder arises if all the ϕ_n are zero while the $f_n \in [-\sigma_f, \sigma_f]$ have finite dispersion and zero average. Such type disorder can be derived from a stochastic potential that features activation

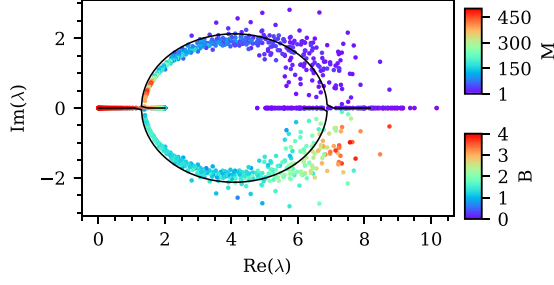


FIG. 3. Representative relaxation spectrum for finite propulsion ($\bar{\phi} = 2$) and TSD ($\sigma_\phi = 1$) with $n = 500$. The eigenvalues are presented in the complex plane. Each associated eigenmode is characterized by various measures: The real and $\text{Im}[\lambda] > 0$ points are color coded by the participation number M , while the conjugate $\text{Im}[\lambda] < 0$ points are color coded by the effective propulsion B . See the text for definitions. The solid line illustrates the spectrum of the nondisordered system (13).

barriers, as discussed by Sinai and followers [32]. The asymmetry of the \mathbf{W} matrix can be gauged away, hence it is similar to a Hermitian matrix, and the relaxation spectrum comes out real. The corresponding eigenstates are Anderson localized.

Propulsion. Without disorder the relaxation spectrum can be found analytically (see Sec. IV). Adding self-propulsion $\bar{\phi}$, unlike drift, leads to a very different route to complexity that is not related to delocalization of the eigenstates. For low self-propulsion the spectrum remains real, while above some critical value the relaxation modes undergo a symmetry-breaking transition. Consequently, a circle of complex eigenvalues appears. In Fig. 3 this circle is indicated by a solid line. If we add weak stochastic disorder the spectrum is blurred, as illustrated in Fig. 3 for TSD and in Fig. 4(a) for CSD.

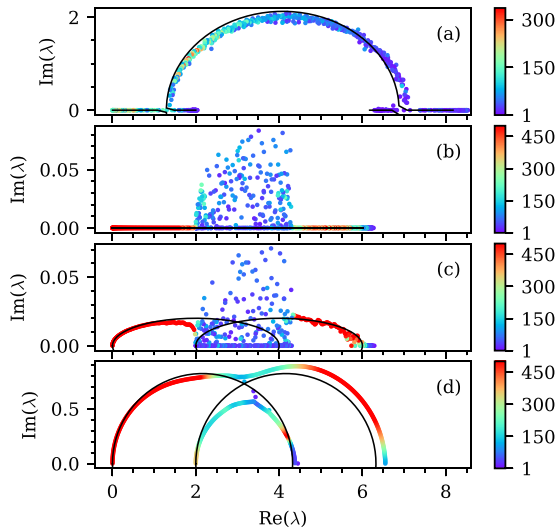


FIG. 4. Representative relaxation spectra. The presentation is the same as in Fig. 3 but with the conjugate eigenvalues excluded. (a) Same propulsion as in Fig. 3 but with CSD ($\sigma_f = 1$) instead of TSD. (b) Same TSD as in Fig. 3, but the average propulsion is zero. (c) Same as (b) but with weak drift ($\bar{f} = 0.02$). (d) Same as (b) but with stronger drift ($\bar{f} = 0.8$).

Topological stochastic disorder. Another route to complexity has to do with mode mixing due to TSD. Even if the propulsion is zero on average, we still can have finite dispersion $\phi_n \in [-\sigma_\phi, \sigma_\phi]$. Then the problem becomes non-Hermitian in a very essential way and part of the spectrum becomes complex. This is illustrated in Fig. 4(b), where we turn off the propulsion for the system of Fig. 3, but keep the TSD. It should be clear that if we turn off the propulsion for the system of Fig. 4(a) the complexity vanishes and we get a real spectrum.

Drift. Without disorder, finite nonzero drift \bar{f} has the same effect as for a single-mode ring, leading to delocalization of the spectrum. We demonstrate in Figs. 4(c) and 4(d) the drift-induced delocalization route to complexity. The drift can delocalize the lower (small $\text{Re}[\lambda]$) and possibly also the upper (large $\text{Re}[\lambda]$) part of the spectrum, where we have single-mode physics. We also see the interplay of the drift and the TSD in the middle part of the spectrum where the two channels overlap. For strong drift the TSD induces an avoided crossing, while for weak drift the TSD-induced complexity predominates.

IV. TOPOLOGICAL SYMMETRY BREAKING

The \mathbf{W} matrix formally operates above a Hilbert space of states whose standard representation is

$$|\psi\rangle = \sum_{n,s} \psi_{n,s} |n,s\rangle. \quad (8)$$

The right eigenvectors of \mathbf{W} are the relaxation modes of the network. The eigenvector that corresponds to the zeroth eigenvalue $\lambda_0 = 0$ is the NESS, while all the other eigenvalues are written as $\{-\lambda_r\}$, with $\text{Re}[\lambda_r] > 0$.

For our geometry, besides the NESS, there is another special mode with the eigenvalue $\lambda = 2$. This can be seen by considering the left eigenvector $|\tilde{2}\rangle = \sum_n (|n, \uparrow\rangle - |n, \downarrow\rangle)$. All the $\lambda \neq 2$ eigenmodes are orthogonal to this special left eigenvector, hence the sum $\sum_n \psi_{n,s}$ has to be equal for both polarizations. Consequently, it is implied that the NESS has equal weight for clockwise and counterclockwise motion, while for all the relaxation modes the sum of amplitudes vanishes for each direction. The same considerations also give the time dependence of the total polarization

$$D = \sum_n D_n = \sum_n (p_{n,\uparrow} - p_{n,\downarrow}). \quad (9)$$

Multiplying Eq. (1) from the left with $|\tilde{2}\rangle$, one obtains a universal decay law $\dot{D} = -2D$.

In the absence of disorder the \mathbf{W} matrix is block diagonal in the basis $|k,s\rangle$, where k is the wave number. For $\bar{\phi} = \bar{f} = 0$ the spectrum consists of two bands along the real axis, namely, $\lambda_{k,+} = 2 - 2\cos(k)$ and $\lambda_{k,-} = 4 - 2\cos(k)$. The existence of the two-channel topology is reflected by having an overlap $2 < \lambda < 4$. Note also that all the eigenvalues are doubly degenerate due to $k \mapsto -k$ symmetry. This holds true also for $\bar{\phi} \neq 0$ (we still keep $\bar{f} = 0$); however, now the spectrum becomes complex. The k th block of the \mathbf{W} matrix is

$$\mathbf{W}^{(k)} = b\sigma_x - ia\sigma_z + c\mathbf{1}, \quad (10)$$

where $b = 1$,

$$a = \left[2 \sinh\left(\frac{\bar{\phi}}{2}\right) \right] \sin(k), \quad (11)$$

$$c = \left[2 \cosh\left(\frac{\bar{\phi}}{2}\right) \right] \cos(k) - \left[1 + 2 \cosh\left(\frac{\bar{\phi}}{2}\right) \right]. \quad (12)$$

The matrix above is similar to a real matrix $b\sigma_z - ia\sigma_y$. Such matrices are usually encountered if there is an antiunitary symmetry such as \mathcal{T} or \mathcal{PT} [13,14]. However, we will stick with the physical representation of Eq. (10). The eigenvalues are either real or come in complex-conjugated pairs, namely,

$$\lambda_{k,q} = -[c \pm \sqrt{b^2 - a^2}], \quad (13)$$

where $q = 1, 2$ labels the lower and upper bands, respectively. The spectrum is real for $|a| < |b|$ and complex for $|a| > |b|$. The latter possibility is realized if $2 \sinh(\bar{\phi}/2) > 1$, leading to a critical value for self-propulsion

$$\phi_c \approx 0.96. \quad (14)$$

Figure 3 shows a representative spectrum for $\bar{\phi} > \phi_c$, where the solid line is based on Eq. (13).

The eigenmodes are labeled as $|k, q\rangle$. In the Bloch sphere representation they reside in the XY or the YZ plane, depending on whether they are associated with real or complex eigenvalues, respectively. Close to the so-called exceptional point ($a = b$) they coalesce into the same Y direction. Disregarding normalization, the eigenmodes are

$$|k, q\rangle = \sum_n e^{ikn} (|n, \uparrow\rangle \pm e^{\pm i\varphi} |n, \downarrow\rangle), \quad (15)$$

where $\tan(\varphi) = a/\sqrt{b^2 - a^2}$. Strong self-propulsion ($a > b$) implies $\varphi = (\pi/2) + i\theta$ with real θ . Consequently, the symmetry with respect to the orientation direction is broken and the modes become polarized, meaning that clockwise modes are separated from counterclockwise modes. On top we note that the $|k, s\rangle$ have a systematic degeneracy for $k \mapsto -k$.

The spectrum of the nondisordered model is further analyzed in Appendix B and is illustrated in a few representative cases in Fig. 5. It is composed of two bands. As discussed above, in the absence of f the bands are deformed into the complex plane provided $\phi > \phi_c$. Figures 5(a)–5(c) illustrate this deformation for increasing values of ϕ . It is important to notice that the $\pm k$ symmetry is not broken, hence each of the two $-\lambda_{k,q}$ trajectories is degenerated and encloses a zero area. This is no longer true if we add a nonzero f . In the latter case the $\pm k$ degeneracy is removed and the $\lambda_{k,s}$ trajectories encloses a finite area.

V. INTRODUCTION OF TSD

We now consider what happens if the illumination is nonuniform. Thus we have TSD with some variation σ_ϕ on top of the average value $\bar{\phi}$. At this point one may wonder whether it is feasible to introduce TSD with zero-average propulsion (the illuminated particles in Fig. 1 are always self-propelled in the direction that they are facing). After little reflection one realizes that it is possible to introduce such TSD if the black-white coating of the particle is reversed in its lower half. Then one can use two sources of illumination: an upper

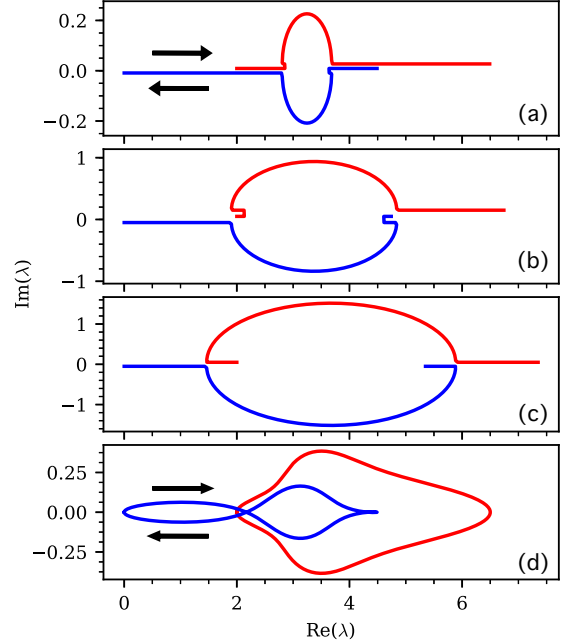


FIG. 5. Bloch spectrum $\lambda_{k,s}$. The two bands are $q = 1$ (blue, lower half-plane) and $q = 2$ (red, upper half-plane). (a)–(c) $f = 0$ and (a) $\phi = 0.98$, (b) $\phi = 1.2$, and (c) $\phi = 1.6$. Note that $\phi_c \approx 0.96$. Equation (13) has been used. For presentation the horizontal pieces of the band have been shifted off the real axis. (d) Same ϕ as in (a) but with an added $f = 0.01$ that lifts the $\pm k$ degeneracy. The black arrows show the direction in which λ_k is changing as $k \in [0, 2\pi]$ is increased from zero and eventually returns.

illumination source that induces self-propulsion (for a given polarization) to one direction and a lower illumination source that induces self-propulsion (for the same polarization) to the other direction. If the two sources are of equal average intensity, the combined effect is to have zero-average propulsion and hence unbiased TSD.

Let us see how the diagonalization procedure for \mathbf{W} is affected in the presence of nonuniform illumination, without assuming any restrictions on the values of $\bar{\phi}$ and σ_ϕ . The standard site basis is $|n, s\rangle$. In order to get rid of the vertical coupling we can switch to the basis $|n, \pm\rangle$, where \pm are the modes that are defined by σ_x . In the absence of propulsion (or TSD) we get two noninteracting chains (see the illustration in Fig. 6). Each chain can be diagonalized, hence we go to the basis $|k, \pm\rangle$. If we introduce disorder and neglect the interband couplings, the spectrum is still real and can be labeled $|\alpha, \pm\rangle$. The α states, unlike the k states, are not free waves and become localized as disorder is increased. In the $|\alpha, \pm\rangle$ basis we can write

$$\mathbf{W} = \mathbf{H} + \mathbf{A}, \quad (16)$$

where \mathbf{H} is Hermitian and \mathbf{A} is an anti-Hermitian matrix due to the self-propulsion. The disorder-induced Hermitian and anti-Hermitian couplings are represented, respectively, by the vertical and diagonal arrows in Fig. 6.

In the absence of disorder \mathbf{A} couples only states with the same k , hence \mathbf{W} takes the block-diagonal form (10), where $\mathbf{A} = -ia\sigma_z$ are the anti-Hermitian interband couplings. Then we get the Bloch eigenstates $|k, q\rangle$, where $q = 1, 2$. With weak TSD the matrix \mathbf{W} is no longer block diagonal. It does

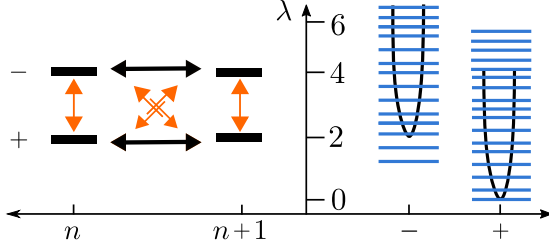


FIG. 6. Diagonalization procedure. We go from the site representation $|n, s\rangle$ of Fig. 1(b) to the mode representation $|\alpha, \pm\rangle$, which is illustrated on the left. The diagonal arrows represent anti-Hermitian couplings due to self-propulsion. The thick double-sided arrows represent the Hermitian hopping elements between cells. The disorder affects all those couplings and also adds vertical hopping elements. The unperturbed diagonal energies are $\lambda = 2$ and $\lambda = 4$. With hopping we get two bands $[0, 4]$ and $[2, 6]$ that are illustrated by the solid line on the right. Neglecting the interband couplings, the spectrum is still real, represented by the blue vertical segments. The complex spectrum appears due to band mixing, as explained in the text.

not require strong disorder in order to induce band mixing. The condition for band mixing is to have A couplings that are larger compared with the level spacing. This is a very easy condition which is implied by perturbation theory (see Appendix C). Consequently, very weak disorder is enough to induce complexity within the range $2 < \text{Re}[\lambda] < 4$. We note that the appearance of disorder-induced Hermitian couplings in H of Eq. (16) does not change this picture: It scrambles the levels of the two bands, but does not alter much their density in the overlap region.

The explanation above illuminates why uniform ϕ_n , unlike random ϕ_n that has the same average intensity, requires a finite threshold (14) in order to induce complexity in the spectrum. Figure 7 displays how the overall fraction of complex eigenstates depends on σ_ϕ , while Fig. 8(a) shows their

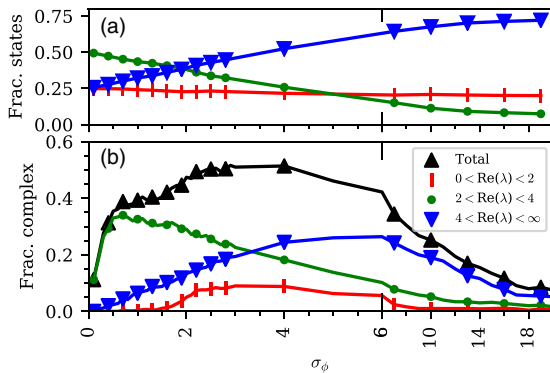


FIG. 7. Spectral distribution of the eigenvalues. (a) Fractions of eigenvalues per spectral window versus the disorder strength σ_ϕ , with $\bar{\phi} = \bar{f} = \sigma_f = 0$. (b) Fraction of complex eigenvalues (out of all eigenvalues) divided into the different spectral windows. In some realizations of the system there are residual complex eigenvalues in the first window ($\text{Re}[\lambda] < 2$), with a small imaginary part. It is not clear whether these are numerical issues or not. The threshold for complexity here is $\text{Im}[\lambda] > 10^{-4}$. The plots are for rings of $N = 500$ cells, with $\phi_n = \alpha_n \sigma_\phi$, where $\alpha_n \in [-1, 1]$ are random numbers. Each point corresponds to a different σ_ϕ , while the α_n are not modified.

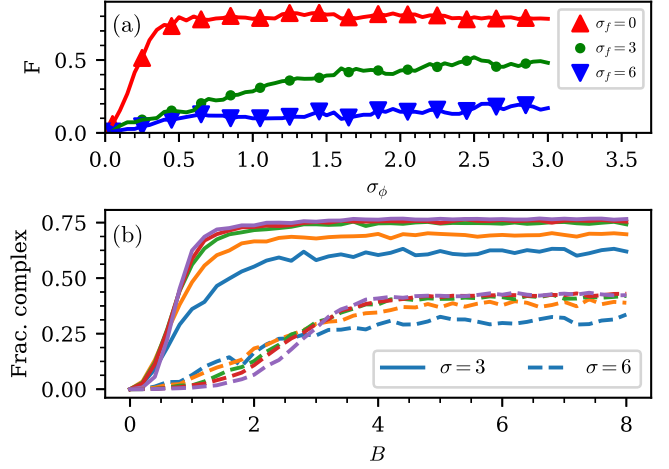


FIG. 8. Fraction of complex eigenvalues. (a) Fraction of complex eigenvalues relative to the number of eigenvalues in the second window ($\text{Re}[\lambda] \in [2, 4]$) for the same ring as in Fig. 7 and for nonzero σ_f too. In the latter case the fraction becomes smaller. (b) Total fraction of complex eigenvalues for a simple ring. Each point in the plots is averaged over 100 realizations. The solid and dashed lines are for $\sigma = 3$ and $\sigma = 6$, respectively. The different lines (from bottom to top at $B > 4$) are for rings of length $L = 5, 10, 20, 30, 60$.

percentage within the range $2 < \lambda < 4$. In order to further explain the consequences of TSD, we now turn to characterize the eigenstates.

VI. TOPOLOGICAL CHARACTERIZATION OF THE EIGENMODES

Assuming square-integrable normalized eigenstates, we formally define $P_{n,s} = |\psi_{n,s}|^2$ and $P_n = \sum_s P_{n,s}$ such that $\sum P_n = \sum P_{n,s} = 1$. Additionally, we define, using a harmonic average, a topological weight for each tile

$$P_n^* = 8 \left[\sum_{\text{site} \in n} P_{n,s}^{-1} \right]^{-1}, \quad (17)$$

where $\text{site} \in n$ refers to the four sites from which the n th tile is formed. The prefactor is chosen such that $P_n^* = 1/N$ for a uniform occupation. A vanishingly small P_n^* means that the n th cell does not form a closed ring.

It is now possible to introduce several measures that characterize a given eigenmode:

$$M = \left[\sum_{n,s} P_{n,s}^2 \right]^{-1}, \quad (18)$$

$$L = \left[\sum_n P_n^2 \right]^{-1}, \quad (19)$$

$$L^* = \left[\sum_n P_n^* \right]^{-1}, \quad (20)$$

$$Q = \sum_{(n,s) \in \text{floor}} P_{n,s}. \quad (21)$$

The first two measures characterize the volume that is occupied by the eigenmodes: M is the number of sites that participate

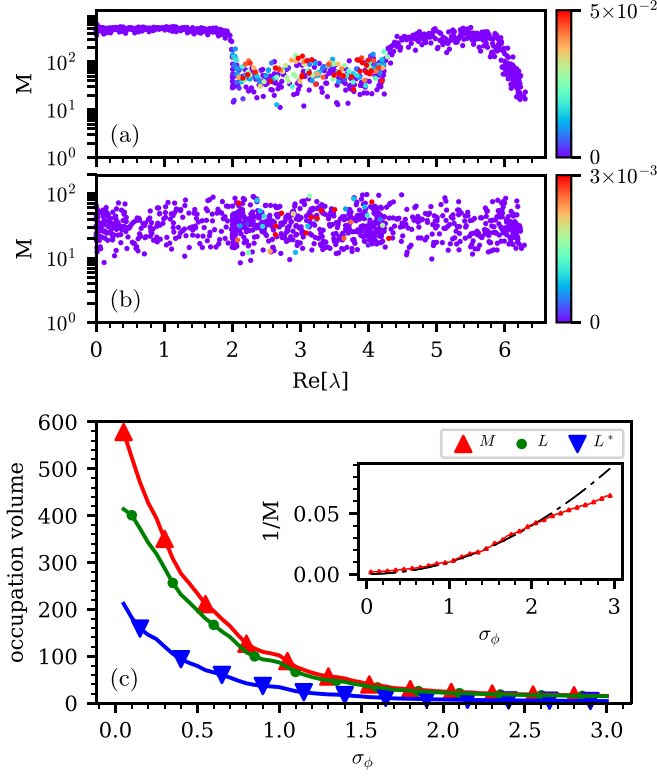


FIG. 9. Participating sites for each eigenmode. (a) Participation number M versus $\text{Re}[\lambda]$ for $\sigma_\phi = 1$ and $\sigma_f = 0.1$, with $\bar{\phi} = \bar{f} = 0$. (b) Same as (a) but with the disorder parameters swapped: $\sigma_f = 1$ and $\sigma_\phi = 0.1$. (c) Various occupations volumes versus σ_ϕ . In (a) and (b) the points are color coded by $\text{Im}[\lambda]$. In (c) each point is an average over all the eigenstates within $2 < \text{Re}[\lambda] < 4$. The inset shows that the inverse localization length has a roughly quadratic dependence on the disorder strength, as in the Anderson model.

in the formation of the eigenmode, while L is the respective localization length. The topological localization length L^* is further discussed below. The definition and the significance of Q will be discussed in the next section.

It is important to realize that the eigenstates might be polarized, meaning that $P_{n,\uparrow} - P_{n,\downarrow}$ is not zero. Polarization can arise either due to symmetry breaking, as discussed in Sec. IV, or due to the formation of a floor level, which is discussed in the next section. For a strictly polarized eigenstate, $L = M$ as opposed to $L = M/2$. Numerical results for M , L , and L^* are presented in Fig. 9.

The topological localization length L^* reflects the effective circulation which is experienced by a given eigenmode. It is determined by the total topological weight $\sum P_n^*$, which is the occupation probability of the region that experiences propulsion. If the total topological weight is much smaller than unity, it means that the non-Hermiticity can be gauged away from the volume that supports the eigenmode, hence the eigenvalue is real (or with very small imaginary part). If the total topological weight is non-negligible, it makes sense to define the effective circulation that is experienced by the eigenmode as follows:

$$B = \sum_n P_n \mathcal{B}_n. \quad (22)$$

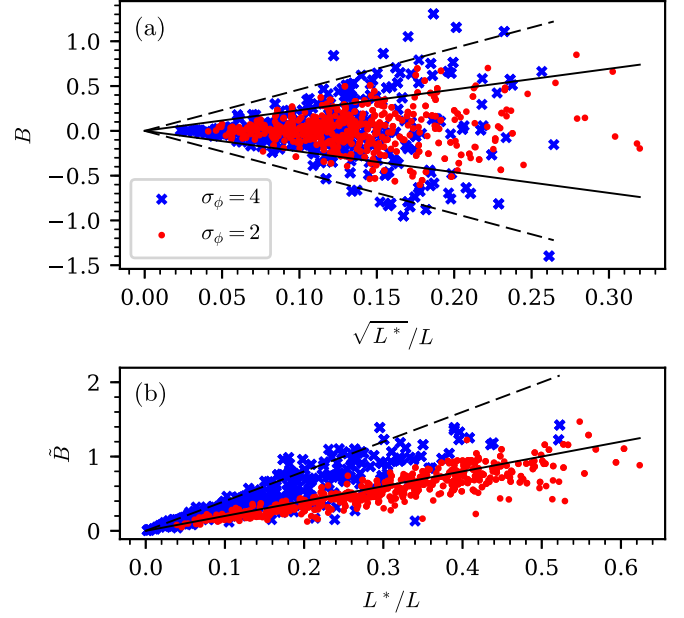


FIG. 10. (a) Effective circulation B of the eigenstates versus their $\sqrt{L^*}/L$, calculated for TSD with $\sigma_\phi = 2$ (red) and $\sigma_\phi = 4$ (blue), as well as $\bar{\phi} = \bar{f} = \sigma_f = 0$. The solid and dashed lines are given by Eq. (23). (b) We define $\tilde{B} = \sum_n P_n |\mathcal{B}_n|$ and verify that it agrees with the estimate $\sim (L^*/L)\sigma_\phi$. Both panels refer to the same set of eigenstates, namely, those that reside in the spectral window $2 < \text{Re}[\lambda] < 4$.

In the absence of disorder, the eigenmodes are uniform and we get $B = 2\bar{\phi}$. In the presence of disorder, the eigenmodes get localized, but if they are uniform within the localization volume (with zero polarization) we still get $B \approx 2\bar{\phi}$. On the other extreme, if the eigenmodes are completely polarized we get a vanishing B . For the intermediate situation, where the eigenmode is supported partially by topologically connected cells and partially by dangling sites, the bare $2\bar{\phi}$ is multiplied by the total topological weight of the eigenmode.

The effective circulation for each state in Eq. (22) can be estimated using the measures L and L^* as follows: By definition, $\sum P_n = L^*/L$. There are L^* terms in the sum; accordingly each term can be estimated as $\sim 1/L$. It follows that B is normally distributed with zero mean and standard deviation

$$\text{SD}(B) = \frac{\sqrt{L^*}}{L} \text{SD}(\mathcal{B}_n) = 2 \frac{(2\sigma_\phi) \sqrt{L^*}}{\sqrt{12} L}. \quad (23)$$

This estimate is tested in Fig. 10. We conjecture that B affects the complexity of the eigenmode. A simple argument that supports this conjecture goes as follows. All the asymmetric transition of dangling bonds can be gauged away using a similarity transformation; hence \mathbf{W} is similar to a matrix $H + A$, where H is real and symmetric and the antisymmetric matrix A is supported only by the topologically connected cells. Multiplying $\mathbf{W}\psi = \lambda\psi$ from the left by ψ^\dagger , we deduce that $\text{Im}[\lambda] = \sum A_{ij} \text{Im}[\psi_i^* \psi_j]$. Consequently, we conclude that from statistical perspective $\text{Im}[\lambda]$ is proportional to the topological weight of the eigenmode.

The above conjecture provides a qualitative explanation for the remarkable difference between TSD and CSD in

Figs. 3 and 4(b), respectively. The transverse scattering of the complex eigenvalues in the former case becomes larger as the localization volume M becomes smaller. Modes with larger B experience (by definition) a larger effective propulsion and therefore they are pushed to a larger radius. The CSD, unlike TSD, does not have a systematic (M -dependent) effect on B , because the B_n are the same for all cells.

One wonders what determines the complexity saturation value of F in Fig. 8(a). For one-dimensional rings that were studied in [22], an analytical treatment has been introduced: For stronger disorder the saturation value becomes smaller, and the approach to this value is smeared, as illustrated in Fig. 8(b). We now use these results to provide a simple explanation for the disorder dependence of F in our model system. A given eigenstate with localization length L exists on a sublattice of size L . Ignoring the detailed bond structure, it can be regarded as an eigenstate of a local ring of size $\sim L$. The σ_f of CSD is by definition the σ disorder for such a local ring, while the σ_ϕ of TSD controls the effective B and hence is analogous to the affinity of the one-dimensional ring. It is therefore expected that σ_f rather than σ_ϕ will have a dominant influence on F . Indeed, we see in Fig. 8(a) that F is sensitive to CSD: Increasing σ_f , unlike increasing σ_ϕ , affects the saturation value. It is true that a further increase of σ_ϕ affects the L of the eigenstates too, but this has almost no implication. To see why, we illustrate in Fig. 8(b) how the F of a simple ring is affected by its length L , which plays the role of localization length in the model under study.

VII. FORMATION OF THE FLOOR LEVEL

In the presence of strong disorder, the floor-level sites are those that serve as sinks for the probability flow [see Fig. 1(c) for illustration]. The NESS and the low-lying relaxation modes mainly occupy these floor-level sites. This hypothesis is established by Fig. 11(a), where we plot the floor occupation Q that has been defined in Eq. (21).

In Fig. 7(a) we show how the eigenvalues are distributed with respect to $\text{Re}[\lambda]$. Generally speaking, we see that the spectrum is stretched upward along $\text{Re}[\lambda]$. This can be easily explained by noting that the diagonal elements of the W matrix become very large for strong disorder, namely,

$$\gamma_{n,s} = 1 + e^{\phi_n/2} + e^{-\phi_{n-1}/2}. \quad (24)$$

However, a careful look reveals that within $\text{Re}[\lambda] \in [0, 2]$ we have an approximate 25% fraction of real eigenvalues, irrespective of the TSD strength. The 25% is not surprising in the limit of weak disorder: Their reality is implied by the band structure. However, their presence and reality persist also for very strong disorder due to the formation of the floor level. From Eq. (24) it follows that for the sink site $1 < \gamma < 3$. Furthermore, as the disorder is increased $\gamma \rightarrow 1$. The hopping between the floor-level states (via high-lying states) leads to the formation of the floor-level band, as established by Fig. 9(c). If we have TSD only, the fraction of floor-level sites is 25%. Adding propulsion, this fraction becomes

$$F_{\text{floor}} = \frac{(\sigma_\phi - \bar{\phi})(\sigma_\phi + \bar{\phi})}{4\sigma_\phi^2}. \quad (25)$$

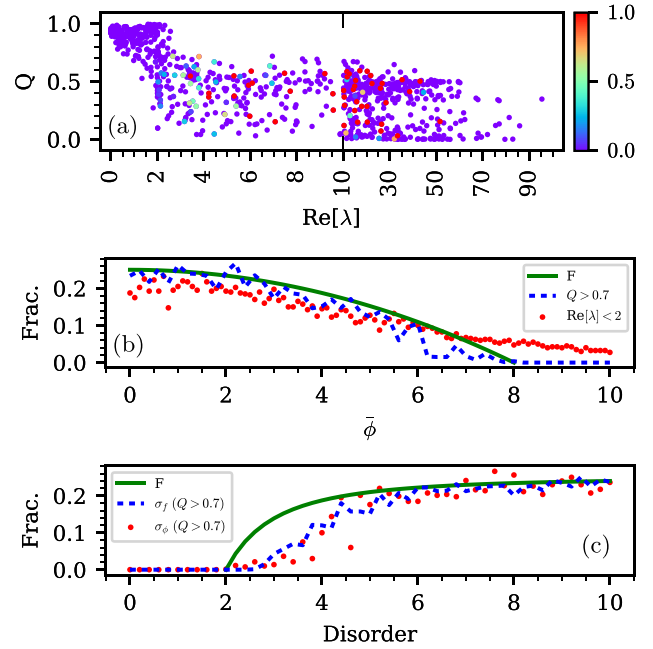


FIG. 11. Floor-level occupation. (a) Floor-level occupation Q versus $\text{Re}[\lambda]$ for $\sigma_\phi = 8$, with $\bar{\phi} = \bar{f} = \sigma_f = 0$. (b) The fraction of floor-level eigenstates drops down from 25% as $\bar{\phi}$ is increased. Floor-level eigenstates are defined as those that have $Q > 0.7$. This is compared with F from Eq. (25) and with the number of states with $\text{Re}[\lambda] < 2$ ($\sigma_\phi = 8$). (c) Fraction of floor-level eigenstates versus σ_f and σ_ϕ . The average propulsion is $\bar{\phi} = 2$.

Consequently, as the disorder is increased we expect a crossover from band-structure implied occupation to the floor-level implied occupation that is illustrated in Fig. 11(a).

Summarizing the TSD case (with zero-average propulsion), we realize that in the absence of disorder, the low-lying eigenmodes are real and nonpolarized because they all belong to a single-channel symmetric mode $|k, +\rangle$ of Eq. (15) with $\varphi = 0$. Increasing the disorder strength, the low-lying eigenmodes occupy only the floor level, hence become polarized (two sites with the same n cannot both serve as sinks), and therefore remain real. Note, however, that we cannot exclude that what we call here real possesses a very small imaginary part due to some residual hopping. On the basis of the numerics it is difficult to obtain a conclusive statement, but from a practical (physical) point of view such a conclusive statement is of no importance.

The same calculation of Eq. (25) holds if we have CSD instead of TSD, namely, with σ_ϕ replaced by σ_f [see Fig. 11(c)]. In contrast with the TSD case, in the strong CSD limit, the sinks come in strongly coupled pairs (two sites with the same n are coupled by a direct vertical bond $w_{\text{flip}} = 1$ rather than via high-lying states with $w_{\text{eff}} \ll 1$). Consequently, half of the floor states have $\lambda > 2$, as implied by Fig. 6. Accordingly, for strong CSD the fraction of states within $\text{Re}[\lambda] \in [0, 2]$ is approximately 12.5% rather than 25%.

VIII. TOPOLOGICAL INDEX

The bulk-edge correspondence principle suggests that localized states should appear at interfaces, connecting regions

of the sample characterized by a different topological number. Below we illuminate the relation between this statement and the floor-level phenomenology that has been introduced in the preceding section.

A translationally invariant sample can be characterized by the winding number

$$w = \frac{1}{2\pi i} \int_0^{2\pi} dk \frac{d}{dk} \ln(\det[W^{(k)}]), \quad (26)$$

which counts the number of times that the eigenenergies encircle the zero energy. Similar to the case of a vanishing band gap in the Hermitian case, the winding number is ill defined when dealing with a conservative system, which always has a $\lambda = 0$ eigenvalue. To circumvent this problem, following [27,28], one has to introduce an F bias, as explained in Appendix B.

Considering an interface between two bulk regions L and R , the topological index is defined as

$$\delta w = w_L - w_R. \quad (27)$$

The interface will localize left (right) zero-energy edge modes if in some finite neighborhood of $F = 0$ the index δw is positive (negative) independently of F . It is important to realize that two bands are not required for observing topological phenomena in non-Hermitian Hamiltonian, which stands in contrast with Hermitian systems [24].

In Appendix B we calculate the topological number of a translationally invariant system given by Eq. (7). We find that a nonzero topological index is associated with interfaces between regions with opposite drift field, independent of the self-propulsion. We further observe that probability density can accumulate also at interfaces between regions that have the same topological number. We point out (see the last paragraph of Appendix B) that the localization in the latter case is less pronounced and is diminished if the length of the nondisordered regions is increased.

The above observations lead to the conclusion that CSD is more effective (compared with TSD) in introducing localized states. The implication of this observation is demonstrated in Fig. 9. We see in Fig. 9(b) a remarkable increase in the likelihood to observe eigenmodes with small M . Another way to phrase this conclusion is to say that eigenmodes that reside in the floor level tend to localize if CSD is dominating and tend to be more extended if TSD is dominating.

IX. SUMMARY AND DISCUSSION

The relaxation modes of a stochastic network can be either overdamped or underdamped depending on whether their λ are real or complex. In a nonactive unbiased disordered network, say a ring, the relaxation is overdamped. However, if we add bias (finite \bar{f}) the low modes become delocalized and we can have underdamped relaxation, which is associated with correlated currents over the whole ring.

The picture of relaxation is much richer if we consider an active network. Without disorder the self-propelled motion (finite $\bar{\phi}$) implies that above a critical value ϕ_c the relaxation modes become polarized due to topological symmetry breaking. Once disorder is taken into account, the picture changes dramatically. An emergent feature of active networks is a new

type of disorder: TSD. Random ϕ_n , unlike uniform ϕ_n , does not require a finite threshold to induce complexity in the spectrum. Either way, in the absence of drift, the underdamped modes are gapped away from the $\lambda = 0$ NESS and characterized by a decay rate that is comparable with the transition rates ($w_b = 1$ in our numerical examples).

Thus we have highlighted that a stochastic network can exhibit three routes to complexity: (a) delocalization of a relaxation mode due to drift, (b) topological symmetry breaking of a relaxation mode, and (c) TSD-induced band mixing of real relaxation modes. The two latter routes to complexity reflect that we are dealing with an active network. These mechanisms are local in some sense and are not associated with global delocalization of the eigenmodes.

Additionally we have shown a theme that distinguishes active matter from passive matter, namely, the emergence of underdamped relaxation modes. Here one should be careful with terminology. Underdamped relaxation has been discussed in the context of active matter [39], but it was associated with the finite inertia of the particles. In contrast, the type of underdamped relaxation that we have discussed here is specifically related to the essence of having an active network, namely, the nonconservative nature of the active stochastic field.

We have presented a detailed investigation of the Fourier-Laplace spectrum for a minimal model of an active network Fig. 1. A time-domain illustration of the dynamics has been displayed in Fig. 2 by means of the local polarization D_n . This illustration shows how the underdamped relaxation due to self-propulsion is blurred by the introduction of disorder. Our objective was to provide a quantitative analysis for this dynamical behavior.

In Sec. VI we have introduced several measures for the characterization of a relaxation mode: the number of lattice sites that support the mode (M), the number of floor-level sites that are involved (Q), their localization lengths (L), and the effective circulation that they experience (B). These measures helped to gain deeper insight into the spectrum.

A few remarks are in order. (i) If the average self-propulsion is zero, the effect of CSD is to stabilize the reality of the spectrum, while TSD induces complexity in the central part of the spectrum via band mixing. (ii) If we further increase the stochastic disorder, the fraction of complex eigenmodes become smaller. There are two issues here: the formation of the floor level due to the effective dilution of the lattice and the fragmentation of the lattice into smaller regions that support the localized eigenmodes. (iii) Opposing the common perspective that connects delocalization and complexity in a single-channel system [15], TSD both makes the spectrum complex and localizes the states. (iv) The effect of TSD can be distinguished from the effect of CSD also if the average self-propulsion is not zero (finite $\bar{\phi}$). The CSD affects democratically all the underdamped modes, while the TSD has a larger effect on the more localized modes.

We can adopt a more general perspective with regard to the floor-level phenomenology, which can be applied for any active network. Strong stochastic disorder, irrespective of its nature, induces lattice dilution, leading to the formation of a floor level that is spanned by the sites that serve as sinks for the stochastic flow. Consequently, the effective dimensionality of the lattice decreases. In our geometry the floor-level sites form

a single-channel chain, hence a robust reality is gained within the floor-level band.

The floor level consists of local sinks of the stochastic flow. In particular, local sinks appear at interfaces between segments characterized by different topological numbers that are determined by the sign of the drift flow, irrespective of the self-propulsion. Still, we observe that probability density can accumulate at interfaces between regions that have the same topological number, e.g., in the presence of TSD and uniform drift. Our numerical analysis shows that the degree of localization in the latter case is less pronounced and smeared away if the nondisordered regions are lengthy. This observation highlights the role of topological protection and its implication on localization in nonequilibrium stochastic flow.

ACKNOWLEDGMENT

D.M. acknowledges support from the Israel Science Foundation (Grant No. 737/14).

APPENDIX A: THE W MATRIX

The matrix W can be regarded as the representation of a non-Hermitian Hamiltonian. It consists of three terms:

$$W = W_{\text{flip}} + W_{\text{hop}} - \sum_{n,s} |n,s\rangle \gamma_{n,s} \langle n,s|.$$

Using the Dirac's bra-ket notation, the explicit expressions for the flipping and hopping terms are

$$W_{\text{flip}} = \sum_n |n, \uparrow\rangle \langle n, \downarrow| + |n, \downarrow\rangle \langle n, \uparrow|,$$

$$W_{\text{hop}} = \sum_{n,s} |n+1,s\rangle \langle n,s| e^{\mathcal{E}_{n,s}/2} + |n,s\rangle \langle n+1,s| e^{-\mathcal{E}_{n,s}/2},$$

with $\mathcal{E}_{n,s}$ that are given by Eq. (3). The decay rates are implied by conservation of probability:

$$\gamma_{n,s} = 1 + e^{\mathcal{E}_{n,s}/2} + e^{-\mathcal{E}_{n-1,s}/2}. \quad (\text{A1})$$

The translation operators $e^{\pm i p}$ of Eq. (7) are defined by $e^{\mp i p} |n,s\rangle = |n \pm 1, s\rangle$. The σ_i operators are defined by $\langle n', s' | \sigma_i | n, s \rangle = (\sigma_i)_{s's} \delta_{n'n}$ in terms of Pauli matrices.

APPENDIX B: THE NONDISORDERED SPECTRUM

Pedagogically, it is useful to consider a single-channel tight-binding model, which is biased by stochastic field f . Additionally, we introduce an F bias [27,28], which affects the off-diagonal rates, but not the diagonal elements. Accordingly,

$$W = -2 \cosh\left(\frac{f}{2}\right) + \sum_{\pm} e^{\pm(f/2+F)} e^{\mp i p}. \quad (\text{B1})$$

The Bloch spectrum is $\{-\lambda_k\}$ with

$$\lambda_k = 2 \cosh\left(\frac{f}{2}\right) - 2 \cosh\left(\frac{f}{2} + F\right) \cos(k) \\ + i 2 \sinh\left(\frac{f}{2} + F\right) \sin(k).$$

This spectrum goes through the origin for $F = 0$, which reflects the existence of the NESS for a conservative matrix.

However, for any nonzero F we can define the winding number w of the $-\lambda_k$ trajectory relative to the origin, namely,

$$w = \text{sgn}[|f + 2F| - f]. \quad (\text{B2})$$

If we have two regions (left and right) that do not have the same f , the difference $\delta w \equiv w_L - w_R$ is well defined in the limit $F \rightarrow 0$ and does not depend on whether we take the limit from the positive or from the negative side. For the topological index of Eq. (27) we get $\delta w = 1$. By the bulk-edge correspondence principle it is implied that a bound state should reside at one of the two interfaces between the two bulk regions which acts as a sink for the flow. (We assume periodic boundary conditions, so the interface is in fact two locations along the ring.)

We now can consider on equal footing our model system (7), where we have two coupled chains, with flip rate $b = 1$. For generality we assume below general b . Here the winding number is calculated from the 2×2 matrix $W^{(k)}$. As in the single-channel example the topological-index calculation requires us to introduce an F bias. The resulting matrix reads

$$W^{(k)} = b \sigma_x + 2 \cosh\left(\frac{f + \phi \sigma_z}{2} + F - ik\right) \\ - b - 2 \cosh\left(\frac{f + \phi \sigma_z}{2}\right) \quad (\text{B3})$$

with eigenvalues $\{-\lambda_k\}$, where

$$\lambda_{k,q} = b - 4 \cosh\left(\frac{\phi}{2}\right) \sinh\left(\frac{f+F-ik}{2}\right) \sinh\left(\frac{F-ik}{2}\right) \\ \mp \sqrt{b^2 + 16 \sinh\left(\frac{\phi}{2}\right)^2 \cosh\left(\frac{f+F-ik}{2}\right)^2 \sinh\left(\frac{F-ik}{2}\right)^2}.$$

The index $q = 1, 2$ corresponds to \mp . Note consistency with Eq. (B1) upon the substitution $b = \phi = 0$. We get two partially overlapping bands provided $b < 2$. The spectrum in a few representative cases has been illustrated in Fig. 5. The $\pm k$ degeneracy is removed if we add a nonzero f , which parallels the single-channel analysis. This has been demonstrated in Fig. 5(c). With an additional F bias the loop looks similar but does not go through the origin. Our analysis shows that the presence of a finite self-propulsion does not alter the topological index, namely, the expression for w is Eq. (B2) as for a single chain.

If we have an interface between two regimes that do not have the same (f, ϕ) bias, there is still a possibility to observe interface states, even if the topological index is zero. This is demonstrated in Fig. 12. We see there that strong localization near the interface is observed only in Fig. 12(a) where the $\delta w \neq 0$. In Fig. 12(b) the high-probability interface and the low-probability interface are mediated by a linear variation in the zero drift ($f = 0$) region, as in Ohmic systems. In Fig. 12(c) the sink in one chain is in fact a saddle, due to its coupling to the other chain, hence the localization is weak. If a longer sample is taken, the hump in Fig. 12(c) is smeared out (not shown).

APPENDIX C: LINEAR ALGEBRA OF NON-HERMITIAN MATRICES

A non-Hermitian operator A has right eigenvectors that satisfy $A|x\rangle = \lambda_x|x\rangle$, where $|x\rangle$ is chosen to have the

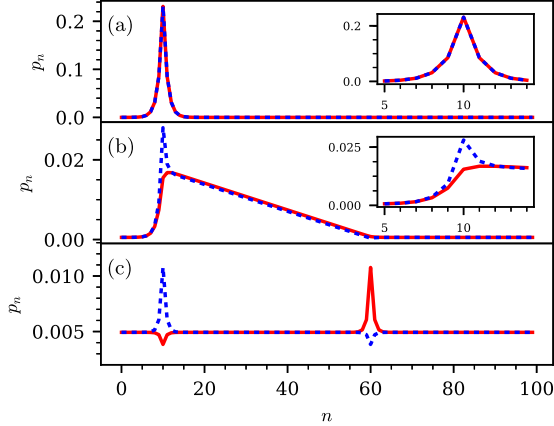


FIG. 12. The NESS for a system that is composed of two regions. The probabilities on the upper and lower chains are plotted as dashed blue and solid red lines. (a) The two regions are with opposite f . The sink interface is located at $n = 10$, while the other interface is at $n = 60$. (b) The $[10, 60]$ region is with ϕ only and the other region is with f only. (c) The two regions are with opposite ϕ . Strong localization near the interface is observed only in case (a), where the topological index is nonzero. The insets of (a) and (b) show close-ups.

normalization $\langle x|x \rangle = 1$. These eigenvectors are in general nonorthogonal: $\langle x|y \rangle \neq 0$. With any right eigenvector we can associate a left eigenvector through the adjoint operator: $A^\dagger|\tilde{x}\rangle = \lambda_x^*|\tilde{x}\rangle$. The right and left eigenvectors form a biorthogonal set and we choose the normalization of the left eigenvectors such that $\langle \tilde{x}|y \rangle = \delta_{x,y}$. For a complete basis $\mathbf{1} = \sum_x |x\rangle\langle \tilde{x}|$. The matrix representation $B_{y,x}$ of an operator B , in the basis $|x\rangle$, is defined via $B|y\rangle = \sum_x B_{x,y}|x\rangle$. One deduces that $B_{x,y} = \langle \tilde{x}|B|y\rangle$ and $B = \sum_{x,y} |x\rangle B_{x,y} \langle \tilde{y}|$.

Given a non-Hermitian matrix H_0 and some perturbation V , we define the right and left unperturbed eigenvectors $|n\rangle$ and $\langle \tilde{m}|$. In this basis H_0 is diagonal with eigenvalues $\lambda_n^{(0)}$. The perturbed eigenvalues in second order are [40]

$$\lambda_n = \lambda_n^{(0)} + \lambda_n^{(1)} + \lambda_n^{(2)}, \quad (\text{C1})$$

$$\lambda_n^{(1)} = \langle \tilde{n}|V|n\rangle, \quad (\text{C2})$$

$$\lambda_n^{(2)} = \sum_m \frac{\langle \tilde{n}|V|m\rangle \langle \tilde{m}|V|n\rangle}{\lambda_n^{(0)} - \lambda_m^{(0)}}. \quad (\text{C3})$$

Note that $V_{n,m}$ will take different forms depending on the normalization of the basis, while the product $V_{n,m}V_{m,n}$ is independent of normalization due to the biorthonormality.

The α eigenstates of Fig. 6 are perturbed versions of k eigenstates. On the basis of standard Fourier-analysis argumentation, the uncertainty in k is determined by the inverse localization length $1/L$. Given an α eigenstate, we can associate with it an average k value. A demonstration of this insight is provided by Fig. 13(a). It displays the magnitude of the anti-Hermitian

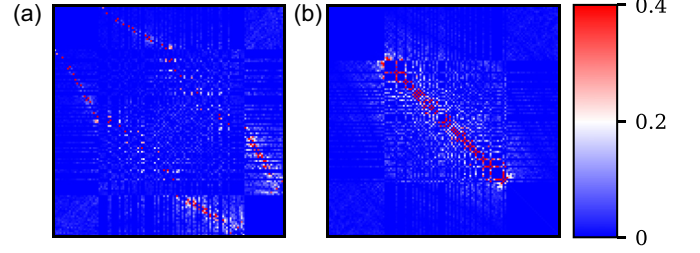


FIG. 13. (a) Image of $|A_{ij}A_{ji}^*|^{1/2}$ in the $|\alpha, \pm\rangle$ basis. The indices are sorted by $\lambda_i^{(0)}$. The propulsion is $\bar{\phi} = 2$, $\sigma_\phi = 0.2$, and $\bar{f} = \sigma_f = 0$. States that have similar k content are strongly coupled. If $\bar{\phi} = 0$ (not displayed) all the couplings becomes comparable as implied by Eq. (C4). (b) Here $\bar{\phi} = 0$ and $\sigma_\phi = 1$. The elements are divided by the eigenvalue differences $|\lambda_i^{(0)} - \lambda_j^{(0)}|$. Large values implies strong coupling that induces strong mixing. Note that in both panels diagonals are excluded. The color scale in (a) is arbitrary, while that of (b) is absolute.

couplings between α states in the presence of propulsion with low TSD. We see that those that have similar k context are strongly coupled. If the average propulsion is switched off, all the elements become comparable in magnitude. Let us find an analytic estimate in the latter case.

The explicit expression for the anti-Hermitian perturbation A is implied by inspection of \mathbf{W}_{hop} , namely,

$$A = \sum_n \sinh\left(\frac{\phi_n}{2}\right) [|n+1\rangle\langle n| - |n\rangle\langle n+1|] \sigma_z.$$

For the matrix elements of the anti-Hermitian perturbation we get $\langle k_2, -|A|k_1, +\rangle = A(q, \bar{k})$, where $q = k_1 - k_2$, $\bar{k} = (k_1 + k_2)/2$, and

$$A(q, \bar{k}) = -\frac{i}{N} \sum_n 2 \sinh\left(\frac{\phi_n}{2}\right) e^{iq(n+1/2)} \sin(\bar{k}). \quad (\text{C4})$$

We can use this expression in order to estimate the anti-Hermitian couplings between α states due to weak TSD. Optionally we can calculate those couplings numerically, as demonstrated in Fig. 13(b). Red implies strong coupling that induces strong mixing.

Eigenvalues in the $\text{Re}[\lambda] \in [2, 4]$ window of an unbiased system become complex whenever the coupling $|A(q, \bar{k})|$ of Eq. (C4) is bigger than (half) the eigenvalue difference between the states. The sum in Eq. (C4) is the sum of N independent random terms, with zero average, and hence for weak TSD, disregarding a prefactor of order unity,

$$|A(q, k)| \approx \frac{\sigma_\phi}{\sqrt{N}} |\sin(k)|. \quad (\text{C5})$$

On the other hand, the spacing within $\text{Re}[\lambda] \in [2, 4]$ is on average proportional to $1/N$. It follows that for large N , the coupling to the spacing ratio is proportional to \sqrt{N} , leading to strong mixing and the emergence of complex eigenvalues, even if the TSD is very weak.

[1] P. Romanczuk, M. Bär, W. Ebeling, B. Lindner, and L. Schimansky-Geier, Active Brownian particles, *Eur. Phys. J. Spec. Top.* **202**, 1 (2012).

[2] A. G. Thompson, J. Tailleur, M. E. Cates, and R. A. Blythe, Lattice models of nonequilibrium bacterial dynamics, *J. Stat. Mech.* (2011) P02029.

- [3] Y. Katz, K. Tunström, C. C. Ioannou, C. Huepe, and I. D. Couzin, Inferring the structure and dynamics of interactions in schooling fish, *Proc. Natl. Acad. Sci. U.S.A.* **108**, 18720 (2011).
- [4] M. C. Marchetti, J.-F. Joanny, S. Ramaswamy, T. B. Liverpool, J. Prost, M. Rao, and R. A. Simha, Hydrodynamics of soft active matter, *Rev. Mod. Phys.* **85**, 1143 (2013).
- [5] A. P. Solon, Y. Fily, A. Baskaran, M. E. Cates, Y. Kafri, M. Kardar, and J. Tailleur, Pressure is not a state function for generic active fluids, *Nat. Phys.* **11**, 673 (2015).
- [6] D. Banerjee, A. Souslov, A. G. Abanov, and V. Vitelli, Odd viscosity in chiral active fluids, *Nat. Commun.* **8**, 1573 (2017).
- [7] J. Katuri, W. E. Uspal, J. Simmchen, A. Miguel-López, and S. Sánchez, Cross-stream migration of active particles, *Sci. Adv.* **4**, eaao1755 (2018); see also <https://www.youtube.com/watch?v=oJ4FMc0J-I4>
- [8] A. Walther and A. H. E. Muller, Janus particles: synthesis, self-assembly, physical properties, and applications, *Chem. Rev.* **113**, 5194 (2013).
- [9] P. M. Wheat, N. A. Marine, J. L. Moran, and J. D. Posner, Rapid fabrication of bimetallic spherical motors, *Langmuir* **26**, 13052 (2010).
- [10] A. M. Menzel, Tuned, driven, and active soft matter, *Phys. Rep.* **554**, 1 (2015).
- [11] C. Maggi, J. Simmchen, F. Saglimbeni, J. Katuri, M. Dipalo, F. De Angelis, S. Sanchez, and R. Di Leonardo, Self-assembly of micromachining systems powered by Janus micromotors, *Small* **12**, 446 (2016); see also <https://www.youtube.com/watch?v=99ockGMSpHI>
- [12] A. Morin, N. Desreumaux, J.-B. Caussin, and D. Bartolo, Distortion and destruction of colloidal flocks in disordered environments, *Nat. Phys.* **13**, 63 (2016).
- [13] M. V. Berry, Physics of nonhermitian degeneracies, *Czech. J. Phys.* **54**, 1039 (2004).
- [14] C. M. Bender, Making sense of non-Hermitian Hamiltonians, *Rep. Prog. Phys.* **70**, 947 (2007).
- [15] N. Hatano and D. R. Nelson, Localization Transitions in Non-Hermitian Quantum Mechanics, *Phys. Rev. Lett.* **77**, 570 (1996).
- [16] N. Hatano and D. R. Nelson, Vortex pinning and non-Hermitian quantum mechanics, *Phys. Rev. B* **56**, 8651 (1997).
- [17] N. M. Shnerb and D. R. Nelson, Winding Numbers, Complex Currents, and Non-Hermitian Localization, *Phys. Rev. Lett.* **80**, 5172 (1998).
- [18] J. Feinberg and A. Zee, Non-Hermitian localization and delocalization, *Phys. Rev. E* **59**, 6433 (1999).
- [19] Y. Kafri, D. K. Lubensky, and D. R. Nelson, Dynamics of molecular motors and polymer translocation with sequence heterogeneity, *Biophys. J.* **86**, 3373 (2004).
- [20] Y. Kafri, D. K. Lubensky, and D. R. Nelson, Dynamics of molecular motors with finite processivity on heterogeneous tracks, *Phys. Rev. E* **71**, 041906 (2005).
- [21] A. Amir, N. Hatano, and D. R. Nelson, Non-Hermitian localization in biological networks, *Phys. Rev. E* **93**, 042310 (2016).
- [22] D. Hurowitz and D. Cohen, Percolation, sliding, localization and relaxation in topologically closed circuits, *Sci. Rep.* **6**, 22735 (2016).
- [23] D. Hurowitz and D. Cohen, Relaxation rate of a stochastic spreading process in a closed ring, *Phys. Rev. E* **93**, 062143 (2016).
- [24] Z. Gong, Y. Ashida, K. Kawabata, K. Takasan, S. Higashikawa, and M. Ueda, Topological phases of non-Hermitian systems, [arXiv:1802.07964](https://arxiv.org/abs/1802.07964).
- [25] W. L. Chan, X. R. Wang, and X. C. Xie, Differences between random-potential and random-magnetic-field localization in quasi-one-dimensional systems, *Phys. Rev. B* **54**, 11213 (1996).
- [26] V. E. Kravtsov, I. V. Lerner, and V. I. Yudson, Random walks in media with constrained disorder, *J. Phys. A: Math. Gen.* **18**, L703 (1985).
- [27] A. Murugan and S. Vaikuntanathan, Topologically protected modes in non-equilibrium stochastic systems, *Nat. Commun.* **8**, 13881 (2017).
- [28] K. Dasbiswas, K. K. Mandadapu, and S. Vaikuntanathan, Topological localization in out-of-equilibrium dissipative systems, [arXiv:1706.04526](https://arxiv.org/abs/1706.04526).
- [29] C. L. Kane and T. C. Lubensky, Topological boundary modes in isostatic lattices, *Nat. Phys.* **10**, 39 (2014).
- [30] T. Reichenbach, T. Franosch, and E. Frey, Exclusion Processes with Internal States, *Phys. Rev. Lett.* **97**, 050603 (2006).
- [31] D. Helbing, Traffic and related self-driven many-particle systems, *Rev. Mod. Phys.* **73**, 1067 (2001).
- [32] Y. G. Sinai, The limiting behavior of a one-dimensional random walk in a random medium, *Theory Probab. Appl.* **27**, 256 (1983).
- [33] B. Derrida, Velocity and diffusion constant of a periodic one-dimensional hopping model, *J. Stat. Phys.* **31**, 433 (1983).
- [34] J.-P. Bouchaud, A. Comtet, A. Georges, and P. Le Doussal, Classical diffusion of a particle in a one-dimensional random force field, *Ann. Phys. (N.Y.)* **201**, 285 (1990).
- [35] J.-P. Bouchaud and A. Georges, Anomalous diffusion in disordered media: Statistical mechanisms, models and physical applications, *Phys. Rep.* **195**, 127 (1990).
- [36] F. J. Dyson, The dynamics of a disordered linear chain, *Phys. Rev.* **92**, 1331 (1953).
- [37] T. A. L. Ziman, Localization and Spectral Singularities in Random Chains, *Phys. Rev. Lett.* **49**, 337 (1982).
- [38] S. Alexander, J. Bernasconi, W. R. Schneider, and R. Orbach, Excitation dynamics in random one-dimensional systems, *Rev. Mod. Phys.* **53**, 175 (1981).
- [39] B.-Q. Ai and F.-G. Li, Transport of underdamped active particles in ratchet potentials, *Soft Matter* **13**, 2536 (2017).
- [40] M. M. Sternheim and J. F. Walker, Non-Hermitian Hamiltonians, decaying states, and perturbation theory, *Phys. Rev. C* **6**, 114 (1972).